11th World Congress on Computational Mechanics (WCCM XI)
5th European Conference on Computational Mechanics (ECCM V)
6th European Conference on Computational Fluid Dynamics (ECFD VI)
E. Oñate, J. Oliver and A. Huerta (Eds)

EDDY VORTICITY IN CAVITATING TIP VORTICES MODELLED BY DIFFERENT TURBULENCE MODELS USING THE RANS APPROACH

TUOMAS P. SIPILÄ[*], ANTONIO SÁNCHEZ-CAJA[*] AND TIMO L. SIIKONEN[†]

[*] VTT Technical Research Centre of Finland
Tietotie 1 A, Espoo
P.O.Box 1000, FI-02044 VTT, Finland
e-mail: tuomas.sipila@vtt.fi, antonio.sanchez@vtt.fi, www.vtt.fi

[†] Aalto University
School of Engineering, Department of Applied Mechanics, Fluid Dynamics
P.O.Box 14400, FI-00076 Aalto
email: timo.siikonen@aalto.fi, www.aalto.fi

Key Words: *Cavitation, Propeller, Tip vortex, Turbulence models, EARSM.*

Summary. VTT Technical Research Centre of Finland and Aalto University have been investigating numerical simulation of cavitating propellers. Special emphasis is placed on the simulation of cavitating tip vortices. The simulations are performed with the $k-\varepsilon$, SST $k-\omega$, and EARSM turbulence models in wetted and cavitating conditions. The calculations are performed in uniform inflow. The propeller performance characteristics and the wake velocities in the wetted conditions were compared to the measurements. Additionally, the simulated cavitation extent on the propeller was compared to the measurements. Good correlation between the tests and simulations were found. The turbulence models gave significant differences to the tip vortex core solutions in wetted and cavitating conditions. The $k-\varepsilon$ model gave high non-dimensional Reynolds stresses both in wetted and cavitating conditions. The anisotropic EARSM model gave the lowest Reynolds stresses in the wetted conditions in the vortex core. In cavitating conditions the SST $k-\omega$, and EARSM models gave very low Reynolds stresses to the vaporous vortex core.

1 INTRODUCTION

Cavitation is a common phenomenon in propeller flows of commercial ships since they are seldom lightly loaded. Cavitation causes several detrimental effects to the ship and the environment, such as vibrations at the stern of the ship, erosion, and noise radiated to the interior of the vessel as well as the underwater environment. Unexpected cavitation behaviour on a propeller may lead, for example, to a decrease of comfort and performance of a cruise ship or a research vessel. Improvements to the propeller or ship wake are difficult and expensive to perform after the ship is built.

Complex dynamic phenomena are involved with cavitation. Although the evaporation and condensation are driven by pressure changes in the liquid medium, the viscous effects play an

important role in the shedding mechanism of sheet cavitation. It is known that sometimes turbulence models applied in the Reynolds averaged Navier-Stokes (RANS) equations produce too much eddy viscosity to the closure of sheet cavities [1]. The increased viscosity at the closure region prevents the natural shedding mechanism of sheet cavitation. Furthermore, the eddy viscosity also damps the strength of the tip vortices.

It is generally known that the $k-\varepsilon$ turbulence models produce more eddy viscosity in the separated flow regions or to the wakes of lifting surfaces than the $k-\omega$ models. In complex flow fields, the isotropic assumption of the eddy viscosity utilized in the two-equation turbulence models is not necessarily valid. To investigate the effect of anisotropic turbulence models on the propeller wake field, and especially on the tip vortex, the Explicit Algebraic Reynolds Stress Model (EARSM) is compared to solutions of the $k-\varepsilon$ and SST $k-\omega$ models.

The simulations are performed with FINFLO, a general-purpose CFD code. The development work of the code started in the late 1980s at Aalto University [2]. VTT Technical Research Centre of Finland has been extending the code for marine applications including free surface and propeller flow modelling since the mid-1990s. Recently, Aalto University has implemented a cavitation model to the code based on Merkle's mass-transfer model [3]. VTT has tested and validated the implemented cavitation model using propeller applications as a reference. The influence of grid resolution and the empirical parameters in the mass-transfer model on the cavitating propeller flows are published in [4,5].

The propeller analysed in this paper is the Potsdam Propeller Test Case (PPTC) propeller of SVA Potsdam [6]. The propeller is a model-size controllable pitch propeller with a diameter $D = 0.250$ m. The skew of the five-bladed propeller is moderate.

The test procedure for the PPTC propeller included determination of the global performance characteristics in open water conditions. The test program contained further tests in a cavitation tunnel. The Laser Doppler Velocimetry (LDV) measurements were performed in the slip-stream of the propeller to determine the location and strength of the tip vortices and the wake of the blades. The LDV measurements were performed in non-cavitating conditions. Furthermore, cavitation tests at varying propeller loads and cavitation numbers were performed. The cavitation extent and the global performance characteristics were recorded.

2 NUMERICAL METHODOLOGY

Flow simulation in FINFLO is based on a solution of the RANS equations by a pressure correction method. The RANS equations are discretized by applying a finite-volume approach. For compressible flows the code uses either Roe's flux-difference splitting or van Leer's flux-vector splitting, whereas in the present incompressible case a third-order upwind-biased scheme is utilized for the convective fluxes. The pressure gradient is centrally differenced, and a second-order central-difference scheme is used for the discretization of the diffusion terms. The solution of the discretized equations is based on an Algebraic Multi-Grid (AMG) method with line Gauss-Seidel smoothing.

For the two-phase flow simulations, it is assumed that the flow is essentially isothermal, decoupling the energy equation from the system. Furthermore, a homogeneous assumption that both phases share the same velocity field is applied, which in turn also simplifies the turbulence modelling. The system of equations can then be expressed as follows:

$$\frac{\partial \rho_m}{\partial t} + \nabla \cdot \rho_m \vec{V} = 0 \tag{1}$$

$$\frac{\partial \rho_m \vec{V}}{\partial t} + \nabla \cdot \rho_m \vec{V}\vec{V} + \nabla p = \nabla \overleftrightarrow{\tau} \tag{2}$$

$$\frac{\partial \alpha_v \rho_v}{\partial t} + \nabla \cdot \alpha_v \rho_v \vec{V} = -\Gamma \tag{3}$$

where ρ is density, $\vec{V}$ is the (shared) velocity, p is the pressure, and $\overleftrightarrow{\tau}$ is the viscous stress tensor. The vapour phase and the mixture of the two phases are depicted by subscripts v and m, respectively. In addition, α_v and Γ are the volume fraction of the vapour phase and the mass transfer term, respectively. Conversely, the liquid phase volume fraction can be expressed as $1 - \alpha_v$.

The cavitation modelling in FINFLO is based on Merkle's mass transfer model [3]:

$$\Gamma_l = \frac{C_{dest}\rho_l \alpha_l \min[0, p - p_{sat}]}{{}^1\!/_2\, \rho_\infty V_\infty^2 (L_{ref}/V_{ref})} + \frac{C_{prod}\rho_v \alpha_v \max[0, p - p_{sat}]}{{}^1\!/_2\, \rho_\infty V_\infty^2 (L_{ref}/V_{ref})} \tag{4}$$

where Γ_l is the mass transfer term, ρ_l is the density of the liquid phase, L_{ref} is the reference length, and V_{ref} is the reference velocity. The chord length and the sectional speed at a radius of $r/R = 0.7$ are considered to be the reference length and speed in the present calculations, respectively, with R depicting the propeller radius. The empirical constants for the evaporation and condensation are given with $C_{dest} = 350$ and $C_{prod} = 350$, respectively. The fluid density far from the propeller is depicted by ρ_∞. The saturation pressure p_{sat} is determined according the Antoine's equation as follows:

$$\log p_{sat} = A - \frac{B}{T_{sat} + C} \tag{5}$$

where A, B, and C are the parameters to be computed from the experimental values, and T_{sat} is the saturation temperature.

The variation of pressure is calculated by summing the density-weighted mass residuals of the gas phase and the liquid phase together. In order to avoid the problems related to the density difference between these two phases, the mass transfer term is pseudo-linearized. The velocity change is determined by combining the mass residual and the explicit momentum residual.

The void fractions are updated at the implicit stage. This is accomplished by transforming the explicit residual to the primitive form and by applying some limitations to the mass transfer rate in order to avoid instabilities during the iteration process. Once the implicit residuals for the pressure δp, the velocity $\delta \vec{V}$, and the mass fraction δm are known, the solution can be obtained using the standard FINFLO pressure correction method. The heat transfer is negligible in ship propeller flows. Even though the energy residuals are determined by the solver, they are set explicitly as zeroes.

The turbulence models applied in the present calculations are Chien's $k - \varepsilon$ [7] and Menter's SST $k - \omega$ [8] turbulence models. In addition, the SST $k - \omega$ model is employed with EARSM [9]. The calculations were performed up to the wall. For this, the first cells'

non-dimensional wall distance is adjusted to $y^+ \sim 1$.

3 GRID AND BOUNDARY CONDITIONS

The cavitation in the investigated condition was stable in the cavitation tests and in the simulations. The square cross section of the tunnel is idealized to be circular in the calculations with an identical cross section area to the actual tunnel. The problem can then be considered symmetric and the quasi-steady approach can be utilized. One fifth of the full domain is modelled due to the symmetry of the five-bladed propeller. A cyclic boundary condition is used at the axial sides of the domain. At the inlet, the velocity boundary condition is used. At the outlet, the pressure boundary condition is applied. At the tunnel walls, a slip surface boundary condition is utilized.

The grid has O-O topology around the blades and H-H topology elsewhere. The grid at the propeller wake field is made iteratively to concentrate cells to the tip vortex location and to the cross-section of the blade wake. The grid is divided into 18 blocks.

Figure 1 shows the surface grid on the propeller blade and a cut of the grid in the propeller slipstream at $x/D = 0.2$ behind the propeller plane. The cut of the grid in the slipstream is coloured by the Reynolds stress component $\rho\overline{u'w'}$. The Reynolds stress component clearly shows the location of the rotational core of the tip vortex and the blade wake.

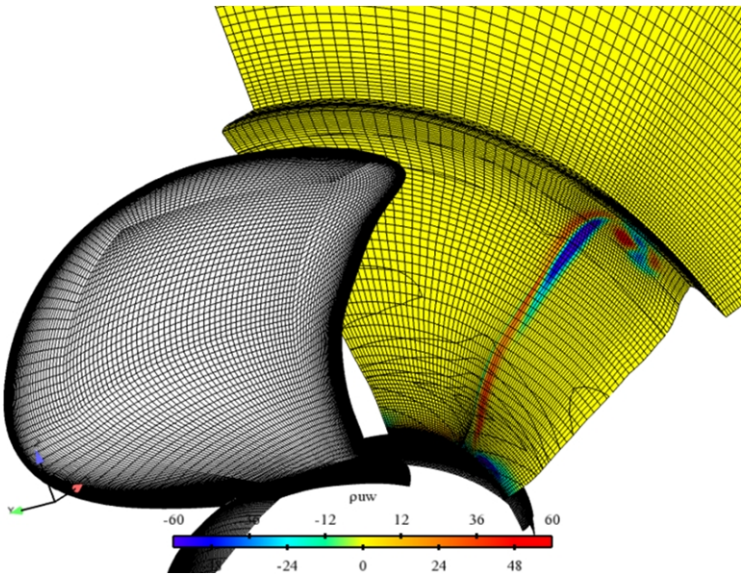

Figure 1: The finest level surface grid on the blade. An axial cut of the grid at $x/D = 0.2$ is also shown. The cut in the wake field is coloured by the Reynolds stress component $\rho\overline{u'w'}$. The result is from the SST $k-\omega$ simulations at $J = 1.225$ in wetted conditions.

The simulations are made on three grid levels. Every second grid point is taken into account in the coarser grid level compared to the finer level grid. The result of the coarser grid level simulation is used as the initial guess in the finer level calculations.

The total number of cells in the finest grid level is 4.3 million. A high grid resolution is set also on the propeller blade to solve the sheet cavity properly. To predict the low pressure peak and hence the cavitation inception accurately, the grid around the leading edge of the blade is

discretized with a very dense grid. Table 1 summarises the grid size details.

Table 1: Grid size details for three grid levels. The number of surface cells is given for one side of the blade.

	Fine grid	Medium grid	Coarse grid
Surface cells chordwise	144	72	36
Surface cells spanwise	104	52	26
Surface cells around leading edge radius	30	15	8
Cells in the tip vortex cross-section	20 × 20	10 × 10	5 × 5
Total number of cells	4 269 568	533 696	66 712

3 RESULTS

4.1 Propeller performance

The propeller open water performance characteristics are calculated at five operating points using the $k-\varepsilon$ turbulence model. The simulation results are compared to the measurements in Figure 2. It is seen that the predicted propeller performance is very close to the measured one over the investigated advance number range.

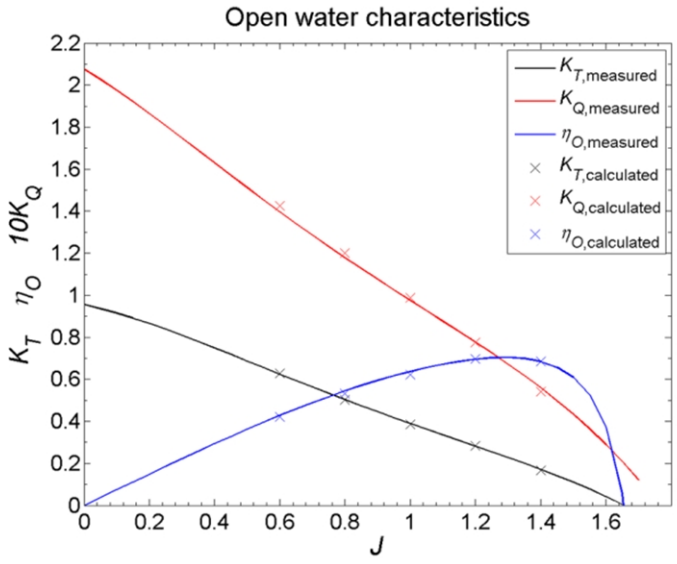

Figure 2: Calculated open water characteristics at different advance numbers. The polynomial fits of the measured open water curves are also shown. Measured data provided by SVA Potsdam.

The propeller advance number J, non-dimensional coefficients for thrust K_T and torque K_Q, and the efficiency η_O are determined as follows:

$$J = \frac{V_A}{nD} \tag{6}$$

$$K_T = \frac{T}{\rho n^2 D^4} \tag{7}$$

$$K_Q = \frac{Q}{\rho n^2 D^5} \tag{8}$$

$$\eta_O = \frac{J}{2\pi}\frac{K_T}{K_Q} \tag{9}$$

where V_A is the propeller advance speed, n is the rate of revolutions, T is the thrust, and Q is the torque.

4.2 Induced velocities in wetted tip vortex core

The Laser Doppler Velocimetry (LDV) measurements of the propeller slipstream were performed in the cavitation tunnel in non-cavitating conditions at J = 1.275. The thrust coefficient was measured as K_T = 0.251The simulations with the $k-\varepsilon$ model were performed according to the thrust identity. The thrust identity was achieved with an advance speed 1.8 % lower than that used in the tests. The simulations with the SST $k-\omega$ and EARSM models were performed with the same J as the $k-\varepsilon$ simulations. The SST $k-\omega$ and EARSM models gave about 3.4 % and 0.1% lower thrust than the $k-\varepsilon$ model, respectively.

Figure 3 shows the measured and calculated axial wake near the tip vortex in the slipstream at axial distance x/D = 0.2 behind the propeller plane. The calculated result is from the SST $k-\omega$ simulations at the finest grid level. It is seen that the tip vortex region is reasonably well predicted. The tip vortex core is slightly higher in the measurements compared to the simulations. The wake field of the propeller is difficult to control accurately in the tests. The wake of the blade, visible as an approximately radial stripe in the figure, is stronger in the simulations than in the measurements.

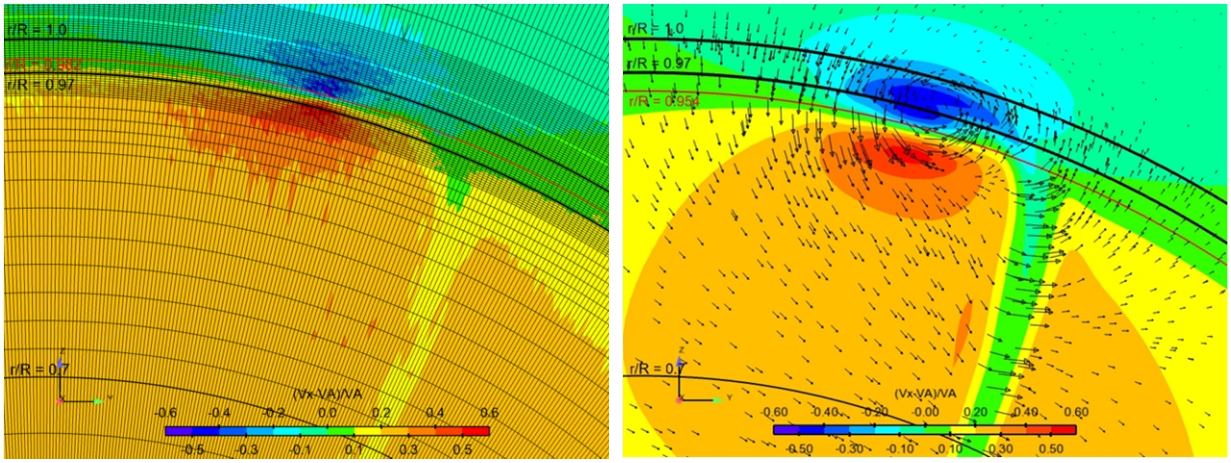

Figure 3: Axial induced velocity near tip vortex at x/D = 0.2. On the left are the measured wake and the spatial resolution of the measurements. On the right is the calculated wake using the SST $k-\omega$ model and the in-plane velocity vectors. The red radii depict the vortex core radius. The black circles depict the radii r/R = 0.7, 0.97 and 1.0. Measured data provided by SVA Potsdam.

Figure 4 shows the circumferential distributions of the velocity components at the vortex core radius at $x/D = 0.2$ behind the propeller plane. The circumferential angle $\theta_{prop} = 0°$ refers to the 12 o'clock position. The circumferential angle increases in the propeller rotational direction. The left diagram in the figure shows the influence of grid resolution on the velocity components in the SST $k-\omega$ simulations. It is seen that the coarsest grid cannot predict the details of the velocity distributions in the tip vortex. The medium grid can find the locations of the peak velocities, but the peaks are significantly deeper at the finest grid level.

The diagram on the right in Figure 4 compares the induced velocity distributions predicted by different turbulence models. The measured distributions are also shown in the diagram. It is seen that the calculated velocities are very close to each other. The peaks in the velocity distributions calculated with the $k-\varepsilon$ model are marginally lower than the results of other turbulence models. The EARSM model gives the highest peaks in the velocity distributions by a small margin. The tip vortex has somewhat smaller radius in the tests than in the calculations.

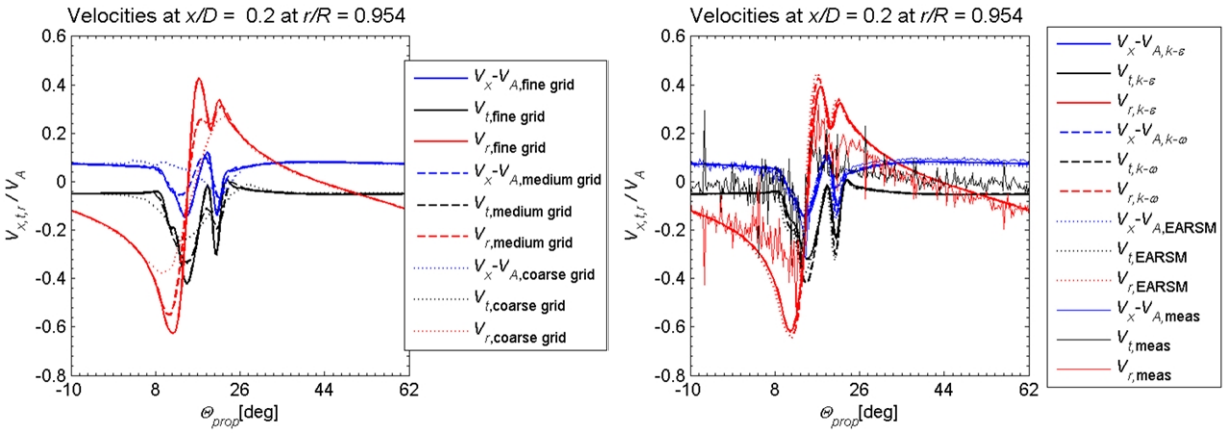

Figure 4: Circumferential distribution of velocity components at $x/D = 0.2$ at the vortex core radius in wetted conditions. On the left are the results calculated with the SST $k-\omega$ model at three grid resolutions. On the right are the results calculated with different turbulence models at the finest grid level together with the measured distributions. Measured data provided by SVA Potsdam.

4.3 Influence of cavitation on tip vortex core

The cavitation tests were performed at $J = 1.025$ where the thrust was $K_T = 0.387$ in the wetted condition. The simulations were again made according to the thrust identity with the tests in the wetted condition. The thrust identity was achieved with 0.6 % lower advance speed with the $k-\varepsilon$ turbulence model compared to the tests. The SST $k-\omega$ and EARSM simulations were performed with the same J value as the $k-\varepsilon$ simulations. The cavitation models are used without modifications for the two-phase flow. The cavitation number in the analysed condition was $\sigma_n = 2.024$. The cavitation number is defined as

$$\sigma_n = \frac{p_\infty - p_{sat}}{\frac{1}{2}\rho(nD)^2} \tag{6}$$

where the pressure in undisturbed flow is depicted by p_∞. The propeller thrust and torque did

not change significantly in the cavitating conditions compared to the wetted conditions in the tests or in the simulations.

Figure 5 shows the observed cavitation extent in the tests and the isosurface of vapour volume fraction α_v = 0.5 in the SST $k-\omega$ simulations. The sheet cavitation occurs at lower radii in the simulations than in the tests. This is most likely caused by cavitation inception delay due to laminar flow separation in the tests at low propeller radii. The surface restricted streamlines on the propeller show that the re-entrant jets reflect from the sheet cavity closure towards the tip of the propeller. Thus, the vapour in the sheet cavity escapes through the tip vortex. Consequently, the sheet cavity is predominantly steady both in the tests and in the simulations. The first modes in the tip vortex cavity shape are similar in the simulations and in the tests. The cavity extent in all simulations is very close to the SST $k-\omega$ result.

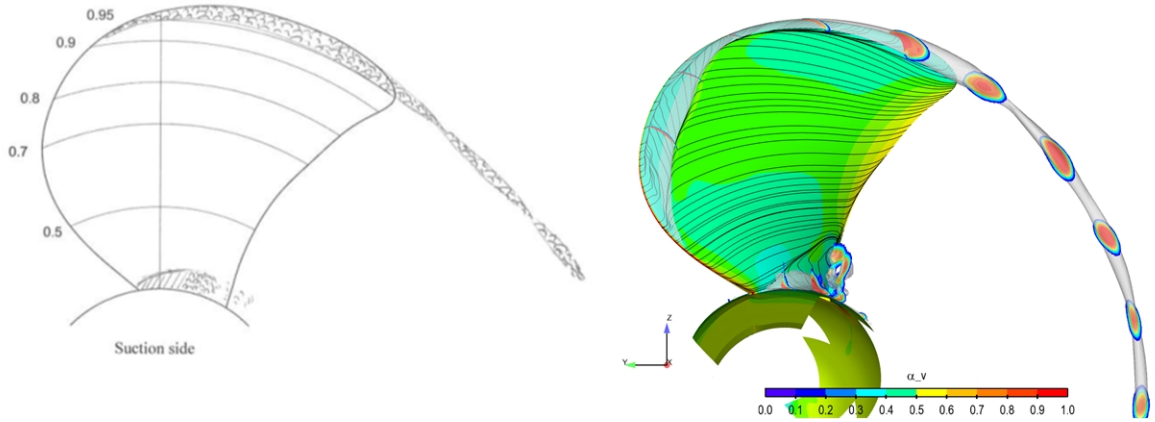

Figure 5: Cavitation extent on propeller. On the left: observations in the tests. On the right: results from the SST $k-\omega$ simulation. The axial cuts inside the cavities are coloured by the vapour volume fraction. The surface restricted streamlines are also shown. The axial cuts have spacing of x/D = 0.05. Tests observations provided by SVA Potsdam.

The circumferential distribution of pressure at the vortex core radius at x/D = 0.2 in wetted and cavitating conditions is shown in Figure 6. The diagram on the left shows the grid dependency of the pressure distribution in the SST $k-\omega$ simulations. It is seen that the pressure minimum in the vortex core changes a lot between the grid levels in the wetted conditions. The pressure is at the vapour pressure at the finest and medium grid levels in the cavitation simulations. At the medium grid level the vapour pressure is reached only by a small margin. At the coarsest grid level the pressure does not reach the vapour pressure in the vortex core.

In the diagram on the right in Figure 6, the circumferential distribution of pressure between different turbulence models is compared in wetted and cavitating conditions. It is seen that the EARSM model gives the lowest pressure in the vortex core in the wetted conditions, whereas the $k-\varepsilon$ model gives the highest pressure. In cavitating conditions, the pressure distributions are similar and cut at the vapour pressure.

Figure 7 shows the circumferential distribution of eddy viscosity and vapour volume fraction at the vortex core radius at an axial plane located at x/D = 0.2 behind the propeller plane. It is seen that the $k-\varepsilon$ model produces significantly more eddy viscosity to the tip

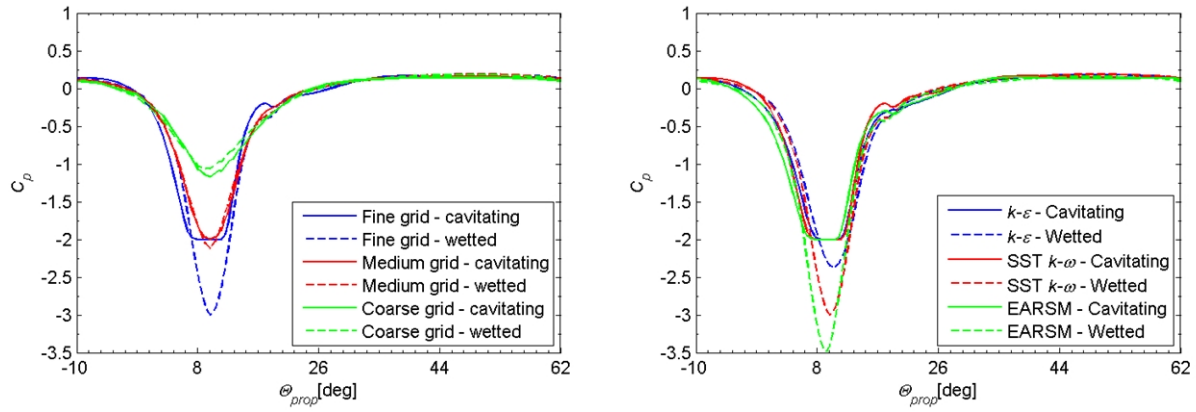

Figure 6: Circumferential pressure distribution at $x/D = 0.2$ behind the propeller at the vortex core radius. On the left: pressure at different grid resolutions in wetted and cavitating conditions using the SST $k-\omega$ turbulence model; on the right: pressure in the finest grid level calculated with different turbulence models.

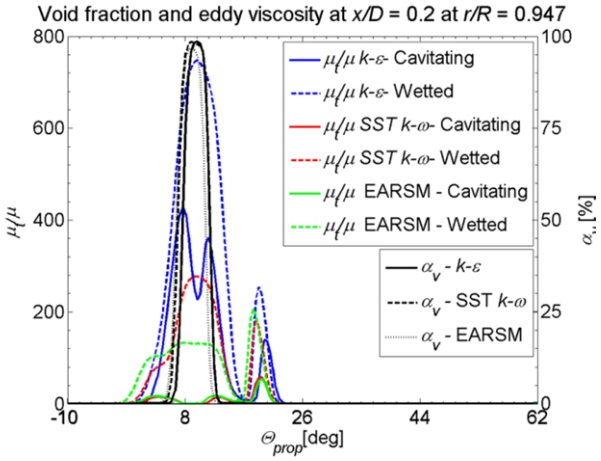

Figure 7: Circumferential distributions of eddy viscosity and void fraction at $x/D = 0.2$ behind the propeller at the vortex core radius. The results are shown for the wetted and cavitating conditions calculated with different turbulence models.

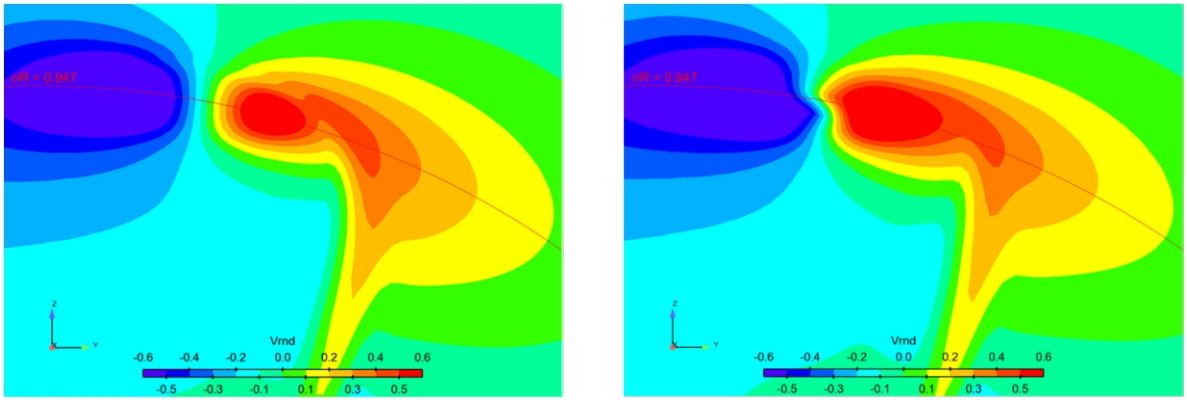

Figure 8: Radial velocity component near the tip vortex at $x/D = 0.2$ behind the propeller. The results are shown for the wetted (left) and cavitating (right) conditions calculated with the $k-\varepsilon$ turbulence model.

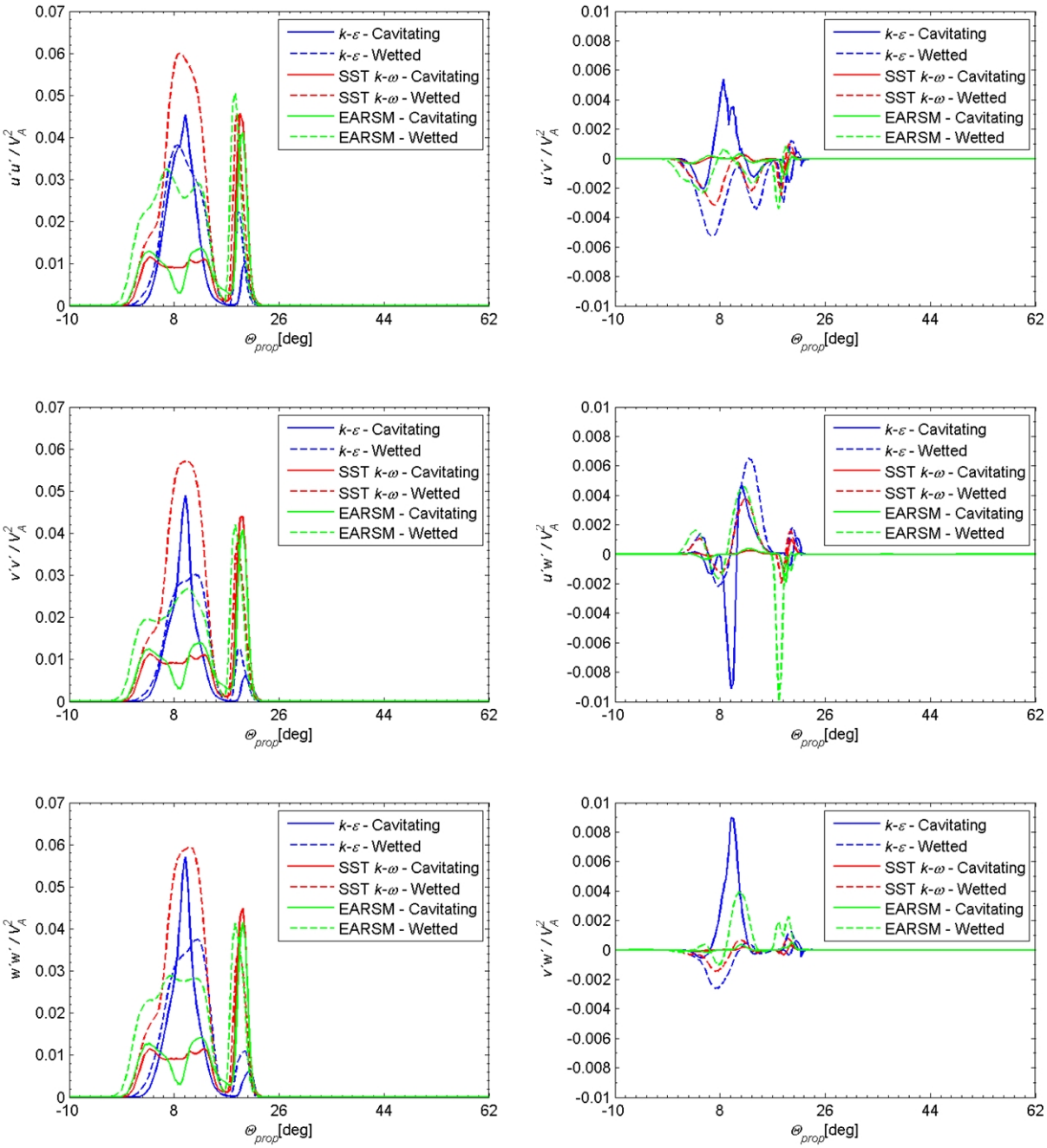

Figure 9: Circumferential distribution of Reynolds stress components in tip vortex core radius at $x/D = 0.2$ behind the propeller. The results are shown for the wetted and cavitating conditions calculated with different turbulence models. On the left: diagonal components; On the right: off-diagonal components.

vortex core in wetted conditions than the other two turbulence models. The sharp peak in the eddy viscosity at about $\theta_{prop} = 20°$ is caused by the blade wake. The eddy viscosity in the EARSM model is lowest in the vortex core in wetted conditions. In cavitating conditions, the $k - \varepsilon$ model gives a high eddy viscosity level in the cavitating vortex core, although the eddy

viscosity decreases in the high void fraction region. The SST $k-\omega$ and EARSM models give low eddy viscosity levels at the outer core of the cavitating vortex. In the vaporous vortex core, the eddy viscosity is practically zero in both models. It is seen that the core of the vortex is filled with almost pure vapour in all the simulations.

The contours of radial velocity component near the tip vortex at an axial plane located at x/D = 0.2 is shown in Figure 8. The results are shown for the wetted and cavitating conditions in the $k-\varepsilon$ simulations. It is seen that the velocity contours become twisted in the cavitation simulation within the vaporous vortex core. The same trend was observed even more strongly in the SST $k-\omega$ and EARSM simulations.

The non-dimensional Reynolds stress components $\overline{u_i'u_j'}/V_A^2$ are shown in Figure 9 at the vortex core radius at an axial plane located at x/D = 0.2 in wetted and cavitating conditions for the three turbulence models analysed. It is seen that the diagonal components of the Reynolds stress tensor are highest with the SST $k-\omega$ model in the wetted conditions. The EARSM and $k-\varepsilon$ models give relative similar diagonal terms for the Reynolds stress tensor in the wetted conditions. The diagonal components of the Reynolds stress increase in cavitating conditions with the $k-\varepsilon$ model. This is opposite to the SST $k-\omega$ and EARSM models, which predict that the diagonal terms decrease significantly in the cavitating tip vortex.

The off-diagonal terms of the Reynolds stress tensor are highest with the $k-\varepsilon$ model in the wetted and cavitating conditions. The EARSM model gives the lowest off-diagonal terms for the Reynolds stress tensor in wetted conditions. In cavitating conditions, the off-diagonal terms of the Reynolds stress tensor are very close to zero in the vaporous tip vortex core with the SST $k-\omega$ and EARSM models. The twist in the velocity contours in the cavitating conditions shown in Figure 8 also causes the off-diagonal terms in the Reynolds stress tensor to shift. Therefore, the off-diagonal terms at the investigated radius have an opposite sign in the cavitating conditions compared to the wetted conditions in the $k-\varepsilon$ simulations.

5 DISCUSSION

The cavitating propeller was analysed with the $k-\varepsilon$, SST $k-\omega$, and EARSM turbulence models. The turbulence models are used as they are in the two-phase flow cases. The results of the simulations were compared to the measured global performance characteristics of the propeller at varying advance numbers. In addition, the calculated induced velocities in the propeller slipstream in non-cavitating conditions were compared to the measured ones. The validation studies showed generally good correlation between the simulation results and the measurements.

A grid refinement study was performed to investigate the effect of the utilized grid resolution on the simulation results in the propeller wake field. It was found out that the finest grid was reasonable for the present study. However, to resolve the low pressure peak in the tip vortex core precisely, the grid resolution should be further refined.

The turbulence models behave very differently in the tip vortex core. In the wetted conditions the $k-\varepsilon$ model gives significantly higher eddy viscosity levels compared to the SST $k-\omega$ and EARSM models. This is reflected in the pressure distribution in the vortex core: the $k-\varepsilon$ model predicts higher pressure to the vortex core than the SST $k-\omega$ model. Furthermore, the anisotropic EARSM model predicts significantly lower pressure to the tip

vortex core than the SST $k-\omega$ model.

In the cavitating tip vortex, the eddy viscosity in the $k-\varepsilon$ simulations remains at high level. In contrast to that, the eddy viscosity in the SST $k-\omega$ and EARSM simulations drops close to zero in the vaporous core of the tip vortex. Only a small level of eddy viscosity is present at the outer radius of the cavitating vortex in the SST $k-\omega$ and EARSM simulations. The non-dimensional Reynolds stresses have naturally similar trends in the simulations to the eddy viscosity. It is interesting to observe that the velocity contours in cavitating conditions become twisted in the constant pressure and nearly inviscid vaporous core of the vortex.

The dimensional Reynolds stress tensor in a mixture of water and vapour is $\rho_m \overline{u_i' u_j'}$. In the cavitating vortex core the mixture contains almost pure vapour. Therefore, the Reynolds stresses are at a low level also in the $k-\varepsilon$ simulations, and almost negligible in the SST $k-\omega$ and EARSM simulations. It is generally known that the turbulence models produce too much viscosity to the vortex cores causing abnormal high diffusion to the vortex strength. Based on this study it can be concluded that this is not an issue in the simulations of cavitating vortices.

REFERENCES

[1] Reboud, J., Stutz, B and Coutier, O. Two-Phase Flow Structure of Cavitation: Experiment and Modeling of Unsteady Effects. *Proceedings of the Third International Symposium on Cavitation* (1998), 203-208, Grenoble, France.

[2] Siikonen, T., Hoffren, J. and Laine, S. A Multigrid LU Factorisation scheme for the thin-layer Navier-Stokes Equations. *Proceeding of 17th ICES Congress* (1990) **90(**6.10.3), 2023-2034, Stockholm, Sweden.

[3] Merkle, C. L., Feng, J., Buelow, P.E.O. Computational Modeling of the Dynamics of Sheet Cavitation. *Proceedings of the Third International Symposium on Cavitation* (1998), 307-311, Grenoble, France.

[4] Sipilä, T., Siikonen, T., Saisto, I. FINFLO RANS-Predictions for Propeller Performance, *Proceedings of Second International Symposium on Marine Propulsors smp'11, Workshop: Propeller performance* (2011), 114-121, Hamburg, Germany.

[5] Sipilä, T., Siikonen, T. RANS predictions of a cavitating tip vortex. *Proceedings of the 8th International Symposium on cavitation CAV2012* (2012), Singapore.

[6] Barkmann, U., Heinke, H.-J. Potsdam Propeller Test Case (PPTC). *Proceedings of the Second International Symposium on Marine Propulsors smp'11, Workshop: Propeller performance* (2011), 36-38, Hamburg, Germany.

[7] Chien, K.-Y. Predictions of Channel and Boundary-Layer Flows with a Low-Reynolds-Number Turbulence Model. *AIAA Journal* (1982) **20(**1), 33-38.

[8] Menter, F. Two-equation eddy-viscosity turbulence models for engineering applications. *AIAA Journal* (1994) **32(**8), 1598-1605.

[9] Wallis, S., Johansson, A.V. An explicit algebraic Reynolds stress model for incompressible and compressible turbulent flows. *Journal of Fluid Mechanics* (2000) **403**, 721-730.